

Electrosynthesis of hydroxylamine *via* plasma-electrochemical cascade pathway using the air and water as raw materials

Xiangdong Kong^{1,3}, Jie Ni^{1,3}, Zhimin Song¹, Zhengwu Yang¹, Jiana Zheng¹, Zifan Xu¹, Lang Qin,¹ Hongliang Li¹, Zhigang Geng^{1,*}, Jie Zeng^{1,2,*}

¹Hefei National Research Center for Physical Sciences at the Microscale, Key Laboratory of Strongly-Coupled Quantum Matter Physics of Chinese Academy of Sciences, Key Laboratory of Surface and Interface Chemistry and Energy Catalysis of Anhui Higher Education Institutes, Department of Chemical Physics, University of Science and Technology of China, Hefei, Anhui 230026, P. R. China

²School of Chemistry & Chemical Engineering, Anhui University of Technology, Ma'anshan, Anhui 243002, P. R. China

³These authors contributed equally to this work.

*Corresponding authors. E-mail: gengzg@ustc.edu.cn (Z.G.); zengj@ustc.edu.cn (J.Z.)

Abstract

The ambient air contains abundant nitrogenous resources that are essential for amine synthesis. Unfortunately, the inert N_2 with stable $N\equiv N$ obstructs the direct synthesis of active nitrogenous compounds from the ambient air. Herein, we developed a sustainable plasma-electrochemical cascade pathway (PECP) powered by renewable electricity for electrosynthesizing one of the active nitrogenous compounds, hydroxylamine (NH_2OH), directly from the ambient air and H_2O . During the PECP, we obtained the nitrate (NO_3^-) solution with a concentration of as high as 120.1 mM. Subsequently, the NO_3^- solution was selectively electroreduced to NH_2OH over Bi-based catalyst. Notably, the faradaic efficiency for NH_2OH reached 81.0% at -1.0 V versus reversible hydrogen electrode. Moreover, we also obtained a state-of-the-art yield rate for NH_2OH of $713.1 \mu mol cm^{-2} h^{-1}$ with selectivity for NH_2OH of 99.3%. Theoretical studies revealed that the Bi(012) facet displayed weaker adsorption energy for the adsorbed NH_2OH intermediate ($*NH_2OH$) in comparison with other kinds of metallic facets, indicating that the Bi catalyst facilitates the desorption of $*NH_2OH$. Meanwhile, the desorption of $*NH_2OH$ was much more favorable than the dissociation of $*NH_2OH$ on the Bi(012) facet, resulting in the highly selective formation of NH_2OH over Bi-based catalysts.

环境空气中含有丰富的氮资源,是胺合成所必需的。遗憾的是,具有稳定 $N\equiv N$ 的惰性 N_2 阻碍了从环境空气中直接合成活性含氮化合物。在此,我们开发了一种以可再生电力为动力的可持续等离子体-电化学级联途径(PECP),可直接从环境空气和 H_2O 中电合成活性含氮化合物之一羟胺(NH_2OH)。在 PECP 过程中,我们获得了浓度高达 120.1 mM 的硝酸盐(NO_3^-)溶液。随后, NO_3^- 溶液在铋基催化剂上被选择性电还原成 NH_2OH 。值得注意的是,与可逆氢电极相比,在-1.0 V 电压下, NH_2OH 的远电效率达到 81.0%。此外,我们还获得了最先进的 NH_2OH 产率($713.1 \mu mol cm^{-2} h^{-1}$)和 99.3% 的 NH_2OH 选择性。理论研究发现,与其他金属面相比,Bi (012) 面对吸附的 NH_2OH 中间体($*NH_2OH$)的吸附能较弱,这表明 Bi 催化剂有利于 $*NH_2OH$ 的解吸。同时,在 Bi (012) 面上, $*NH_2OH$ 的解吸比 $*NH_2OH$ 的解离更有利,因此在 Bi 基催化剂上形成 NH_2OH 的选择性很高。

Keywords: utilization of ambient air, electrosynthesis of NH_2OH , plasma fixation of N_2 , NO_3^-

electroreduction.

Introduction

Hydroxylamine (NH_2OH), as an important nitrogenous feedstock with high reactivity, has been widely applied for the synthesis of nitrogen-containing compounds in the chemical, agrochemical, and pharmaceutical fields¹⁻⁶. The traditionally industrial methods for the synthesis of NH_2OH include the Raschig method, nitric monoxide (NO) reduction method, and nitric acid (HNO_3) reduction method (Fig. 1a)⁷⁻⁹. Nonetheless, the Raschig method employs both highly corrosive and polluted sulfur dioxide as the reductant with producing a large amount of $(\text{NH}_4)_2\text{SO}_4$ as the by-product. As for both NO and HNO_3 reduction methods, H_2 derived from the petrochemical process and noble metal materials (Pt , Pd , Ru , and Rh) have been used as proton source and catalysts, respectively, greatly increasing the cost for NH_2OH production⁹⁻¹¹. Although other paths such as acetoxime method, methyl-ethyl ketone method, and hydrogen peroxide oxidation method have been developed for the potential synthesis of NH_2OH ¹²⁻¹⁵, they have also been confronted with the high cost of reactants or the low yield for NH_2OH production (Fig. 1b). Moreover, it is worth noting that the nitrogen sources for all these traditionally synthetic methods for NH_2OH originate from the energy-intensive Haber-Bosch process, leading to serious carbon footprint and energy consumption issues¹⁶⁻¹⁸. In order to circumvent the aforementioned drawbacks, it is of pivotal significance to exploit both more practical and sustainable alternatives for NH_2OH synthesis.

羟胺 (NH_2OH) 作为一种具有高反应活性的重要含氮原料, 已被广泛应用于化工、农用化学品和医药领域含氮化合物的合成 1-6。合成 NH_2OH 的传统工业方法包括 Raschig 法、一氧化氮 (NO) 还原法和硝酸 (HNO_3) 还原法 (图 1a) 7-9。不过, Raschig 法使用腐蚀性强、污染严重的二氧化硫作为还原剂, 并产生大量 $(\text{NH}_4)_2\text{SO}_4$ 作为副产品。至于 NO 和 HNO_3 还原法, 则分别使用石油化工过程中产生的 H_2 和贵金属材料 (铂、钯、钌和铑) 作为质子源和催化剂, 从而大大增加了 NH_2OH 的生产成本 9-11。虽然其他途径, 如乙酰肼法、甲基乙基酮法和过氧化氢氧化法, 也有可能合成 NH_2OH ¹²⁻¹⁵, 但它们也面临着反应物成本高或 NH_2OH 产率低的问题 (图 1b)。此外, 值得注意的是, 所有这些传统 NH_2OH 合成方法的氮源都来自高能耗的 Haber-Bosch 工艺, 导致严重的碳足迹和能源消耗问题 16-18。为了避免上述弊端, 开发更实用、更可持续的 NH_2O 替代品具有重要意义。

In this work, we developed a plasma-electrochemical cascade pathway (PECP) for the renewable NH_2OH electrosynthesis from the ambient air and H_2O (Fig. 1c). Such PECP included the preparation of nitrate (NO_3^-) from the ambient air by plasma synthesis and the production of NH_2OH towards NO_3^- electroreduction. In contrast to the traditionally synthetic paths, the electrosynthesis driven by renewable electricity using both green and abundant H_2O as proton source paves a promising avenue for the sustainable production of NH_2OH . To overcome the limitation of the extremely low reactivity for the direct N_2 electrochemical activation¹⁹⁻²¹, we exploited a homemade plasma discharge device for the highly efficient N_2 activation into the oxynitride (NO_x) by straightly using the ambient air as feeding gas. After steadily absorbing the NO_x with H_2O for 30 min, we obtained the NO_3^- solution with the concentration of as high as 120.1 mM. Subsequently, the NO_3^- solution was selectively electroreduced to NH_2OH using Bi nanoparticles loaded on carbon fiber paper (denoted as Bi NPs/CFP) as the catalyst. At applied potential of -1.0 V versus reversible hydrogen electrode (vs. RHE), Bi NPs/CFP exhibited a faradaic efficiency (FE) for NH_2OH of 81.0%. Notably, a yield rate for NH_2OH of $713.1 \mu\text{mol cm}^{-2} \text{ h}^{-1}$ was achieved over Bi NPs/CFP at -1.2 V vs. RHE. Based on density functional theory (DFT) calculations, the Bi(012) facet displayed a weaker adsorption energy (E_{ads}) for the adsorbed NH_2OH intermediate ($^*\text{NH}_2\text{OH}$) in comparison with other kinds of metallic facets, suggesting that Bi catalyst brings benefit to the desorption of $^*\text{NH}_2\text{OH}$. Meanwhile, the desorption of $^*\text{NH}_2\text{OH}$ was much more favorable than the dissociation of $^*\text{NH}_2\text{OH}$ on the Bi(012) facet, resulting in the highly selective formation of NH_2OH towards NO_3^- electroreduction.

在这项工作中，我们开发了一种等离子体-电化学级联途径（PECP），用于从环境空气和 H_2O 中电合成可再生的 NH_2OH （图 1c）。这种 PECP 包括通过等离子合成从环境空气中制备硝酸盐（ NO_3^- ），以及通过 NO_3^- 电还原生产 NH_2OH 。与传统的合成途径相比，利用绿色和丰富的 H_2O 作为质子源，由可再生电力驱动的电合成为 NH_2OH 的可持续生产铺平了道路。为了克服 N_2 直接电化学活化反应活性极低的限制¹⁹⁻²¹，我们利用自制的等离子体放电装置，直接使用环境空气作为进料气体，将 N_2 高效活化成氧化氮化物（ NO_x ）。用 H_2O 稳态吸收 NO_x 30 分钟后，我们得到了浓度高达 120.1 mM 的 NO_3^- 溶液。随后，使用负载在碳纤维纸上的 Bi 纳米粒子（称为 Bi NPs/CFP）作为催化剂，选择性地将 NO_3^- 溶液电还原为 NH_2OH 。在对可逆氢电极（vs. RHE）施加 -1.0 V 的

电位时, Bi NPs/CFP 对 NH_2OH 的电解效率 (FE) 为 81.0%。值得注意的是, Bi NPs/CFP 在 -1.2 V 对 RHE 条件下的 NH_2OH 产率达到了 $713.1 \mu\text{mol cm}^{-2} \text{h}^{-1}$ 。根据密度泛函理论 (DFT) 计算, 与其他金属面相比, Bi (012) 面对吸附的 NH_2OH 中间体 ($^*\text{NH}_2\text{OH}$) 的吸附能 (E_{ads}) 较弱, 这表明 Bi 催化剂有利于 $^*\text{NH}_2\text{OH}$ 的解吸。同时, $^*\text{NH}_2\text{OH}$ 的解吸比 $^*\text{NH}_2\text{OH}$ 在 Bi(012) 面上的解离更为有利, 从而导致 NH_2OH 在 NO_3^- 电还原过程中的高选择性形成。

Results and discussion

Plasma synthesis of NO_3^- from the ambient air and H_2O . As indicated by the reaction mechanism and previous reports on the discharge activation of N_2 ²²⁻²⁴, it is of vital importance to increase the collision probability between N and O radicals for improving the yield rate of NO_x . Because the dissociation of inert N_2 into N radicals take place within the energy-concentrated region of the plasma discharge device, the overlapping zone between the electric arc and the ambient air is positively correlated with the activation rate of N_2 . Hence, we designed a plasma discharge device equipped with multiple parallel tips to enlarge the overlapping zone for the efficient activation of N_2 (Supplementary Fig. 1). Typically, a high-voltage power supply with an input alternating current (AC) voltage of 50 V was adopted to generate an output AC voltage of 10 kV between the tips. To verify the feasibility of N_2 plasma fixation from ambient air on the homemade plasma discharge device, we performed a qualitative analysis. When gaseous substances produced by the plasma discharge were purged into the aqueous absorbent containing 0.02 mM methyl orange, the absorbent gradually turned from light yellow to salmon pink within 30 s (Fig. 2, a, b, and Supplementary Video). In contrast, when the ambient air was directly bubbled into the absorbent, no significant change was observed for the color of the absorbent during the absorption time of 10 min (Supplementary Fig. 2). These results suggested that the acidic NO_x produced from the plasma discharge was absorbed in aqueous solution to form HNO_3 .

等离子体从环境空气和 H_2O 中合成 NO_3^- 。根据 N222-24 的放电活化反应机理和以往的报告, 提高 N 和 O 自由基之间的碰撞概率对于提高 NO_x 的产率至关重要。由于惰性 N_2 离解成 N 自由基发生在等离子体放电装置的能量集中区域, 电弧与环境空气之间的重叠区与 N_2 的活化率呈正相关。因此, 我们设计了一种配备多个平行尖端的等离子体放电

装置，以扩大重叠区，从而有效活化 N_2 （附图 1）。通常情况下，采用输入交流电（AC）电压为 50 V 的高压电源，在尖端之间产生 10 kV 的输出交流电压。为了验证自制等离子体放电装置从环境空气中固定 N_2 等离子体的可行性，我们进行了定性分析。当等离子体放电产生的气态物质被净化到含有 0.02 mM 甲基橙的水吸收液中时，吸收液在 30 秒内从浅黄色逐渐变成橙红色（图 2, a, b 和补充视频）。相反，当环境空气直接进入吸收剂时，吸收剂的颜色在 10 分钟的吸收时间内没有明显变化（补充图 2）。这些结果表明，等离子体放电产生的酸性氮氧化物被水溶液吸收后生成了 HNO_3 。

To evaluate the performance for N_2 fixation using the plasma discharge device, we quantified the yield of NO_3^- . After the absorption of gaseous products in 30 mL of H_2O , the concentration for NO_3^- was analyzed by ion chromatography. The flow rate of the ambient air was a key parameter for optimizing the efficiency of N_2 fixation. Fig. 2c shows the concentration for NO_3^- after the 5-min plasma discharge under various flow rates of the ambient air. The concentrations for NO_3^- were monotonically increased when the flow rates of the ambient air were modulated from 20 to 200 standard cubic centimeter per minute (SCCM). Under the flow rate of 200 SCCM, the concentration for NO_3^- reached as high as 20.3 mM. To meet the requirement of the high-yield preparation of NO_3^- , we chose the flow rate of 200 SCCM as the optimum condition for the continuous discharge process. As shown in Fig. 2d, the concentrations for NO_3^- were almost linearly accumulated in 30 mL of absorbent after continuous discharge for various times. Notably, the concentration for NO_3^- reached as high as 120.1 mM for 30 min. We further conducted the cyclic stability tests on the plasma discharge device. Each cycle was continuously discharged for 30 min. During 20 cyclic stability tests, the concentrations for NO_3^- in the absorbent were always higher than 115.3 mM (Fig. 2e). The as-obtained aqueous NO_3^- solution can be directly fed for the NO_3^- electroreduction process.

为了评估使用等离子放电装置固定 N_2 的性能，我们对 NO_3^- 的产量进行了量化。在 30 mL H_2O 中吸收气态产物后，用离子色谱法分析了 NO_3^- 的浓度。环境空气的流速是优化 N_2 固定效率的关键参数。图 2c 显示了在不同流速的环境空气中，等离子体放电 5 分钟后的 NO_3^- 浓度。当环境空气的流速从每分钟 20 标准立方厘米（SCCM）调节到 200 标准立方厘米（SCCM）时， NO_3^- 的浓度呈单调上升趋势。在 200 SCCM 的流速下， NO_3^- 的浓度高达 20.3 mM。为了满足高产制备 NO_3^- 的要求，我们选择了 200 SCCM 的流量

作为连续排放过程的最佳条件。如图 2d 所示, 连续排放不同时间后, 30 mL 吸收液中的 NO_3^- 浓度几乎呈线性累积。值得注意的是, 在 30 分钟内, NO_3^- 的浓度高达 120.1 mM。我们进一步对等离子体放电装置进行了循环稳定性测试。每个循环连续放电 30 分钟。在 20 次循环稳定性测试中, 吸收剂中的 NO_3^- 浓度始终高于 115.3 mM (图 2e)。获得的 NO_3^- 水溶液可直接用于 NO_3^- 电还原过程。

NO_3^- electroreduction into NH_2OH . Bi NPs/CFP was adopted as the catalyst towards NO_3^- electroreduction. Typically, Bi NPs/CFP was obtained *via* the magnetron sputtering of Bi disk on CFP with direct current deposition. As revealed by the scanning electron microscope (SEM) measurements (Fig. 3a and Supplementary Fig. 3), Bi nanoparticles were closely packed on the surface of CFP. The SEM images of the cross-sectional Bi NPs/CFP showed a clear interface between CFP and the layer the Bi nanoparticles (Supplementary Fig. 4). The magnified SEM image of the cross-sectional Bi NPs/CFP suggested that the thickness for the layer of Bi nanoparticles was around 730 nm (Fig. 3b). Based on the SEM energy dispersive X-ray (EDX) elemental mapping analysis, the layered-stack structure was also verified by the distinct elemental distributions (Fig. 3c). As shown by the high-angle annular dark field scanning transmission electron microscope (HAADF-STEM) measurement, the interplanar spacing of 0.328 nm for an individual Bi nanoparticle was assigned to (012) facet of metallic Bi (Fig. 3d). In the X-ray diffraction (XRD) spectra, except for the characteristic peaks of CFP, the new peaks at 22.5° , 27.2° , 38.0° , 39.6° , 44.6° , 45.9° , and 59.3° were indexed to the (003), (012), (104), (110), (015), (006), and (107) facets of hexagonal Bi (JCPDS No. 41-1246), respectively (Fig. 3e). As shown by Raman spectra, the characteristic peaks at 70.5 and 97.0 cm^{-1} for Bi NPs/CFP were attributed to the E_g and A_{1g} stretching modes of the metallic Bi-Bi bond, respectively (Fig. 3f). Supplementary Fig. 5 shows the X-ray spectroscopy (XPS) spectra. Bi NPs/CFP exhibited two peaks at 162.4 and 157.0 eV in the Bi 4f XPS spectrum, assigned to the $4f_{5/2}$ and $4f_{7/2}$ of Bi^0 species, respectively. By contrast, no obvious signal was detected in the Bi 4f XPS spectrum of CFP.

NO_3^- 电还原成 NH_2OH 。Bi NPs/CFP 被用作 NO_3^- 电还原的催化剂。通常情况下, Bi NPs/CFP 是通过磁控溅射将 Bi 圆片溅射到 CFP 上并以直流沉积的方式获得的。扫描电子显微镜 (SEM) 测量显示 (图 3a 和补充图 3), Bi 纳米粒子紧密地堆积在 CFP 表面。Bi NPs/CFP 横截面的扫描电子显微镜图像显示, CFP 与 Bi 纳米粒子层之间存在清晰的界

面(补充图 4)。Bi NPs/CFP 横截面的放大 SEM 图像表明, Bi 纳米粒子层的厚度约为 730 nm (图 3b)。根据扫描电镜能量色散 X 射线(EDX)元素图谱分析, 层叠结构也得到了明显的元素分布验证(图 3c)。高角度环形暗场扫描透射电子显微镜(HAADF-STEM)测量结果表明, 单个 Bi 纳米粒子的平面间距为 0.328 nm, 属于金属 Bi 的 (012) 面(图 3d)。在 X 射线衍射(XRD)光谱中, 除 CFP 的特征峰外, 在 22.5°、27.2°、38.0°、39.6°、44.6°、45.9° 和 59.3° 处的新峰分别与六方 Bi (JCPDS 编号 41-1246) 的 (003)、(012)、(104)、(110)、(015)、(006) 和 (107) 面有关(图 3e)。拉曼光谱显示, Bi NPs/CFP 在 70.5 和 97.0 cm^{-1} 处的特征峰分别归因于金属 Bi-Bi 键的 E_g 和 A_{1g} 伸展模式(图 3f)。补充图 5 显示了 X 射线光谱(XPS)图谱。在 Bi 4f XPS 光谱中, Bi NPs/CFP 在 162.4 和 157.0 eV 处出现了两个峰, 分别归属于 BiO 物种的 4f_{5/2} 和 4f_{7/2}。相比之下, 在 CFP 的 Bi 4f XPS 光谱中没有检测到明显的信号。

The NO_3^- electroreduction measurements were carried out in an H cell using 0.5 M H_2SO_4 solution containing 0.1 M NO_3^- as the catholyte. The chronoamperometry electrolysis was conducted to quantitatively analyze the catalytic performance of NO_3^- electroreduction. During NO_3^- electroreduction, an argon (Ar) stream with a flow rate of 20 SCCM was used as the shielding gas to insulate the catholyte from the air. Meanwhile, the gaseous products were carried out by Ar stream for quantification *via* an online gas chromatography (GC). To eliminate the interference of the O-H groups in H_2O to the N-H groups in NH_2OH , we adopted an excess amount of glyoxylic acid ($\text{C}_2\text{H}_2\text{O}_3$) to capture NH_2OH *via* a spontaneous oximation process. As determined by ^1H nuclear magnetic resonance (NMR) measurements, NH_2OH was quantified based on the C-H group of glyoxylic acid oxime ($\text{C}_2\text{H}_3\text{NO}_3$) (Supplementary Fig. 6). Besides, NH_3 was also quantitatively analyzed by ^1H NMR. At all applied potential from -0.6 to -1.2 V vs. RHE, NH_2OH was determined as the predominant product for NO_3^- electroreduction over Bi NPs/CFP (Fig. 4a and Supplementary Fig. 7). H_2 was determined to be the main gaseous by-product (Supplementary Fig. 8). Notably, the FE for NH_2OH over Bi NPs/CFP reached up to 81.0% at -1.0 V vs. RHE. At -1.2 V vs. RHE, the yield rate for NH_2OH over Bi NPs/CFP was as high as $713.1 \mu\text{mol cm}^{-2} \text{h}^{-1}$ (Fig. 4b). Such value represents the highest yield rate for NH_2OH among recent reports²⁵⁻²⁸ (Supplementary Table 1). In addition, the selectivity for NH_2OH over Bi NPs/CFP was always higher than 99.3% at all applied potential. According to a series of

control experiments, Bi served as the active species for the NO_3^- electroreduction into NH_2OH (Supplementary Figs. 9-11).

以含 0.1 M NO_3^- 的 0.5 M H_2SO_4 溶液为电解质, 在 H 型电池中进行了 NO_3^- 电还原测量。为了定量分析 NO_3^- 电还原的催化性能, 还进行了计时器电解。在 NO_3^- 电还原过程中, 使用流量为 20 SCCM 的氩气流作为屏蔽气体, 使阴溶液与空气隔绝。同时, 气态产物被氩气流带走, 通过在线气相色谱仪 (GC) 进行定量。为了消除 H_2O 中 O-H 基团对 NH_2OH 中 N-H 基团的干扰, 我们采用了过量的乙醛酸 ($\text{C}_2\text{H}_2\text{O}_3$), 通过自发氧化过程捕获 NH_2OH 。通过 ^1H 核磁共振 (NMR) 测定, NH_2OH 是根据乙醛酸肟 ($\text{C}_2\text{H}_3\text{NO}_3$) 的 C-H 基团来定量的 (附图 6)。此外, 还通过 ^1H NMR 对 NH_3 进行了定量分析。与 RHE 相比, 在 -0.6 至 -1.2 V 的所有应用电位下, NH_2OH 被确定为 NO_3^- 电还原的主要产物, 而不是 Bi NPs/CFP (图 4a 和补充图 7)。 H_2 被确定为主要的气态副产物 (补充图 8)。值得注意的是, 与 RHE 相比, 在 -1.0 V 条件下, Bi NPs/CFP 上 NH_2OH 的 FE 高达 81.0%。在 -1.2 V 对 RHE 时, Bi NPs/CFP 上的 NH_2OH 产率高达 $713.1 \mu\text{mol cm}^{-2} \text{ h}^{-1}$ (图 4b)。在最近的报告 25-28 中, 该值代表了最高的 NH_2OH 产率 (补充表 1)。此外, 在所有应用电位下, NH_2OH 对 Bi NPs/CFP 的选择性始终高于 99.3%。根据一系列对照实验, Bi 是 NO_3^- 电还原成 NH_2OH 的活性物种 (补充图 9-11)。

To evaluate the catalytic stability of Bi NPs/CFP, we carried out the continuous NO_3^- electroreduction. A 5-h continuous chronopotentiometry electrolysis at 100 mA cm^{-2} was firstly conducted to explore the accumulation of NH_2OH in the catholyte. As show in Fig. 4c, the accumulated concentrations for NH_2OH were almost linearly increased with the average yield rate for NH_2OH higher than $456.5 \mu\text{mol cm}^{-2} \text{ h}^{-1}$. The accumulated concentration for NH_2OH reached as high as 77.7 mM (Fig. 4d). In the meantime, the FE and selectivity for NH_2OH were always higher than 73.4% and 99.3% during 5-h electrolysis, respectively (Supplementary Fig. 12). We carried out cyclic stability tests to further study the catalytic stability of Bi NPs/CFP towards NO_3^- electroreduction. Specifically, each cycle was continuously electrolyzed at 100 mA cm^{-2} for 5 h. In the period of 12 cycles with the total electrolytic duration of 60 h, the product selectivity for NH_2OH was still higher than 99.2% (Fig. 4e). Moreover, the average yield rate for NH_2OH fluctuated within the error range of 6.0% during 12 cyclic tests. The solid $2\text{NH}_2\text{OH} \cdot \text{H}_2\text{SO}_4$ products of 1.887 g with separation efficiency of 89.9% was achieved from the

360 mL of catholyte after 12 cyclic tests of NO_3^- electroreduction (Insert Fig. 4e). Based on the structural characterizations (Supplementary Figs. 13-16), the metallic Bi species in Bi NPs/CFP were preserved after the 60-h electrolysis.

为了评估 Bi NPs/CFP 的催化稳定性,我们进行了连续 NO_3^- 电还原。首先在 100 mA cm^{-2} 下进行了 5 小时的连续时变电解,以探究 NH_2OH 在电解液中的积累情况。如图 4c 所示, NH_2OH 的累积浓度几乎呈线性增长, NH_2OH 的平均产率高于 $456.5 \text{ } \mu\text{mol cm}^{-2} \text{ h}^{-1}$ 。 NH_2OH 的累积浓度高达 77.7 mM (图 4d)。同时,在 5 小时的电解过程中, NH_2OH 的 FE 和选择性始终分别高于 73.4% 和 99.3% (附图 12)。为了进一步研究 Bi NPs/CFP 对 NO_3^- 电还原的催化稳定性,我们进行了循环稳定性测试。具体而言,每个循环在 100 mA cm^{-2} 下连续电解 5 小时。在总电解时间为 60 小时的 12 个循环中, NH_2OH 的产物选择性仍高于 99.2% (图 4e)。此外,在 12 次循环试验中, NH_2OH 的平均产率在 6.0% 的误差范围内波动。经过 12 次 NO_3^- 电还原循环测试,从 360 毫升阴溶液得到了 1.887 克 $2\text{NH}_2\text{OH}\cdot\text{H}_2\text{SO}_4$ 固体产品,分离效率为 89.9% (插图 4e)。根据结构表征 (补充图 13-16), Bi NPs/CFP 中的金属 Bi 物种在 60 小时电解后得以保留。

To unravel the intrinsic reason for the high activity and selectivity for NH_2OH over Bi NPs/CFP, we investigated the reaction mechanism of NO_3^- electroreduction. Fig. 5a shows a typical pathway for the formation of NH_2OH and NH_3 derived from the electroreduction of NO_3^- . Among these steps, the selectivity of the production for NH_2OH or NH_3 was determined by the adsorbed behavior of $^*\text{NH}_2\text{OH}$. In general, NH_3 has been reported as the final product for NO_3^- electroreduction over the most of metallic catalysts^{20,29-31}. We thus adopted various metallic materials including nickel (Ni) foil, copper (Cu) foil, silver (Ag) foil, tin (Sn) foil, and platinum (Pt) foil as cathodic catalysts to uncover the formation mechanism of NH_2OH towards NO_3^- electroreduction. As shown in Fig. 5b, Bi NPs/CFP exhibited both the highest FE and yield rate for NH_2OH among all these catalysts. According to the structural characterizations, the exposed surface for the Ni foil, Cu foil, Ag foil, Sn foil, Pt foil, and Bi NPs were enclosed by cubic Ni(100), cubic Cu(100), cubic Ag(100), tetragonal Sn(211), cubic Pt(100), and hexagonal Bi(012) facets, respectively (Supplementary Fig. 17). Hence, we conducted spin polarized DFT calculations to investigate the adsorbed behaviors of $^*\text{NH}_2\text{OH}$ by adopting representative Ni(100), Cu(100), Ag(100), Sn(211), Pt(100), and Bi(012) facets as model slabs (Supplementary Figs. 18). As shown in Fig. 5c, the Bi(012) facet displayed an E_{ads} for $^*\text{NH}_2\text{OH}$ of 0.01 eV, much

weaker than the other counterparts. This result indicated that the desorption of $^*\text{NH}_2\text{OH}$ on Bi catalyst was more favorable in comparison with these on the other metallic catalysts. We further simulated the transformation of $^*\text{NH}_2\text{OH}$ on the Bi(012) facet to gain in-depth understanding for the selective production of NH_2OH over Bi catalyst (Supplementary Fig. 19). As shown in Fig. 5d, the Gibbs free energy change was calculated to be -0.73 eV for the desorption of $^*\text{NH}_2\text{OH}$ into NH_2OH , suggesting that $^*\text{NH}_2\text{OH}$ desorption was a thermodynamically spontaneous process on the Bi(012) facet. Nevertheless, the energy barrier for $^*\text{NH}_2\text{OH}$ dissociation into adsorbed NH_2 ($^*\text{NH}_2$) and adsorbed OH ($^*\text{OH}$) was calculated as high as 0.85 eV on the Bi(012) facet. These results suggested that NH_2OH path was more favorable than NH_3 path towards NO_3^- electroreduction over Bi catalyst. As such, the weak adsorption of $^*\text{NH}_2\text{OH}$ was responsible for the selective formation of NH_2OH towards NO_3^- electroreduction.

为了揭示 Bi NPs/CFP 对 NH_2OH 具有高活性和高选择性的内在原因，我们研究了 NO_3^- 电还原的反应机理。图 5a 显示了 NO_3^- 电还原生成 NH_2OH 和 NH_3 的典型路径。在这些步骤中，产生 NH_2OH 或 NH_3 的选择性取决于 $^*\text{NH}_2\text{OH}$ 的吸附行为。一般来说， NH_3 是大多数金属催化剂 20、29-31 电还原 NO_3^- 的最终产物。因此，我们采用了多种金属材料，包括镍 (Ni) 箔、铜 (Cu) 箔、银 (Ag) 箔、锡 (Sn) 箔和铂 (Pt) 箔作为阴极催化剂，来揭示 NH_2OH 在 NO_3^- 电还原过程中的形成机理。如图 5b 所示，在所有催化剂中，Bi NPs/CFP 的 NH_2OH FE 和产率都是最高的。根据结构表征，Ni 箔、Cu 箔、Ag 箔、Sn 箔、Pt 箔和 Bi NPs 的暴露面分别由立方 Ni (100)、立方 Cu (100)、立方 Ag (100)、四方 Sn (211)、立方 Pt (100) 和六方 Bi (012) 面围成（补充图 17）。因此，我们采用具有代表性的 Ni(100)、Cu(100)、Ag(100)、Sn(211)、Pt(100) 和 Bi(012) 面作为模型板，进行了自旋极化 DFT 计算，以研究 $^*\text{NH}_2\text{OH}$ 的吸附行为（补充图 18）。如图 5c 所示，Bi(012)刻面对 $^*\text{NH}_2\text{OH}$ 的 E_{ads} 值为 0.01 eV ，比其他对应刻面弱得多。这一结果表明，与其他金属催化剂相比，Bi 催化剂对 $^*\text{NH}_2\text{OH}$ 的解吸更为有利。我们进一步模拟了 $^*\text{NH}_2\text{OH}$ 在 Bi(012) 面上的转化过程，以深入了解在 Bi 催化剂上选择性生产 NH_2OH 的过程（补图 19）。如图 5d 所示，计算得出 $^*\text{NH}_2\text{OH}$ 解吸成 NH_2OH 的吉布斯自由能变化为 -0.73 eV ，这表明 $^*\text{NH}_2\text{OH}$ 解吸在 Bi(012) 面上是一个热力学自发过程。然而，根据计算， $^*\text{NH}_2\text{OH}$ 在 Bi(012) 面上解离成吸附的 NH_2 ($^*\text{NH}_2$) 和吸附的 OH ($^*\text{OH}$) 的能垒高达 0.85 eV 。这些结果表明，在 Bi 催化剂上， NH_2OH 路径比 NH_3

路径更有利于 NO_3^- 的电还原。因此， $^*\text{NH}_2\text{OH}$ 的弱吸附性是 NH_2OH 在 NO_3^- 电还原过程中选择性形成的原因。

Conclusions

In summary, we developed a PECP for renewable NH_2OH electrosynthesis. Combining the plasma discharge with electroreduction processes, we significantly promoted both the N_2 fixation and NH_2OH synthetic efficiency, implementing the sustainable NH_2OH synthesis from the ambient air and H_2O . During PECP, we obtained a yield rate for NH_2OH of as high as $713.1 \mu\text{mol cm}^{-2} \text{ h}^{-1}$ with a selectivity for NH_2OH of 99.3%. We believe that the PECP for the electrosynthesis of NH_2OH could not only upgrade the NH_2OH synthetic technology but also promote N fixation. This work opens up a new route for the green and sustainable electrosynthesis of NH_2OH , which also provides rational guidelines for the renewable synthesis of other nitrogenous compounds.

总之，我们开发了一种用于可再生 NH_2OH 电合成的 PECP。结合等离子体放电和电还原过程，我们显著提高了 N_2 固定和 NH_2OH 合成效率，实现了从环境空气和 H_2O 中合成可再生 NH_2OH 。在 PECP 过程中，我们获得了高达 $713.1 \mu\text{mol cm}^{-2} \text{ h}^{-1}$ 的 NH_2OH 产率， NH_2OH 的选择性高达 99.3%。我们相信，用 PECP 电合成 NH_2OH 不仅能提升 NH_2OH 合成技术，还能促进氮的固定。这项作为 NH_2OH 的绿色可持续电合成开辟了一条新途径，也为其他含氮化合物的可再生合成提供了合理的指导。

Methods

Chemicals and materials

Concentrated sulfuric acid (H_2SO_4 , 98wt%), concentrated nitric acid (HNO_3 , 68wt%), ethanol (EtOH), concentrated hydrochloric acid (HCl, 37wt%), acetone, titanium (Ti) mesh, Ni foil, Cu foil, Ag foil, Sn foil, and Pt foil were purchased from Sinopharm Chemical Reagent Co., Ltd. Aqueous glyoxylic acid solution ($\text{C}_2\text{H}_2\text{O}_3$, 50wt%), iridium(III) chloride hexahydrate ($\text{YCl}_3 \cdot 3\text{H}_2\text{O}$) were purchased from Aladdin Chemistry Co., Ltd. (Shanghai, China). Methyl sulfoxide (d_6 -DMSO, 99.9atom% D), 1-Propanesulfonic acid 3-(trimethylsilyl) sodium salt (DSS), and Nafion 115 membrane were purchased from Sigma-Aldrich. Bi disk (99.995%, $\phi 50.8 \times 3$ mm) was purchased from ZhongNuo Advanced Material (Beijing) Technology Co., Ltd. The deionized H_2O was produced using a Millipore Milli-Q grade with a resistivity of 18.2 $\text{M}\Omega \text{ cm}$. All the chemicals were used as received without any further purification.

浓硫酸 (H_2SO_4 , 98wt%)、浓硝酸 (HNO_3 , 68wt%)、乙醇 (EtOH)、浓盐酸 (HCl, 37wt%)、丙酮、钛网、镍箔、铜箔、银箔、锡箔和铂箔购自国药集团化学试剂有限公司。乙醛酸水溶液 ($\text{C}_2\text{H}_2\text{O}_3$, 50wt%)、六水合氯化铱 (III) ($\text{YCl}_3 \cdot 3\text{H}_2\text{O}$) 购自阿拉丁化学有限公司 (中国上海)。(中国上海) 购买。甲基亚砷 (d_6 -DMSO, 99.9atom% D)、1-丙磺酸 3-(三甲基硅基) 钠盐 (DSS) 和 Nafion 115 膜购自 Sigma-Aldrich。Bi 盘 (99.995%, $\phi 50.8 \times 3$ mm) 购自中诺先进材料 (北京) 科技有限公司。去离子水使用 Millipore Milli-Q 级仪器生产, 电阻率为 18.2 $\text{M}\Omega \text{ cm}$ 。所有化学试剂均按原样使用, 未经进一步纯化。

Plasma synthesis of NO_3^- from the ambient air and H_2O

In the standard plasma synthetic process, the ambient air with controllable flow rates was pumped into the homemade plasma discharge device. A high-voltage generator was adopted as power supply with the input AC voltage and power of 50 V and 20 W, respectively. During the plasma synthetic process, the as-obtained NO_x were absorbed by a homemade absorption tower using deionized H_2O as the absorbent. The concentration of NO_3^- after the absorption of NO_x was quantitatively analyzed by ion chromatography.

等离子体合成环境空气和 H_2O 中的 NO_3^-

在标准等离子体合成过程中, 可控流量的环境空气被泵入自制的等离子体放电装置。高压发生器用作电源, 输入交流电压和功率分别为 50 V 和 20 W。在等离子体合成过程中,

得到的氮氧化物被自制的吸收塔吸收，吸收塔使用去离子水作为吸收剂。吸收氮氧化物后的 NO_3^- 浓度通过离子色谱法进行定量分析。

Synthesis of Bi NPs/CFP

The Bi NPs/CFP was synthesized based on our previous report with a slight modification³². Typically, Bi disk and CFP were used as target material and substrate, respectively. Direct current magnetron sputtering was conducted with a constant current of 50 mA under an Ar atmosphere (2.4×10^{-3} mbar, 20 SCCM) at room temperature for 3000 s. After the magnetron sputtering process, the as-obtained sample was directly used as the catalyst for NO_3^- electroreduction measurements.

Bi NPs/CFP 的合成

Bi NPs/CFP 是在我们之前的报告基础上稍加修改合成的³²。通常，Bi 盘和 CFP 分别用作靶材料和基底。磁控溅射过程结束后，得到的样品直接用作 NO_3^- 电还原测量的催化剂。

Pretreatment of metallic foils

Ni foil, Cu foil, Ag foil, Sn foil, and Pt foil were immersed in EtOH and ultrasonically cleaned for at least 10 min. EtOH was then replaced by acetone to conduct the ultrasonic cleaning process. After three repeated treatments, the working electrodes were immersed in 10wt% of HCl solution for 10 min to remove surface oxide. After HCl treatment, the working electrodes were washed with deionized H_2O and stored in acetone for further use.

金属箔的预处理

将镍箔、铜箔、银箔、锡箔和铂箔浸入乙醇中，超声波清洗至少 10 分钟。然后用丙酮代替 EtOH 进行超声波清洗。重复三次处理后，将工作电极浸入 10wt% 的盐酸溶液中 10 分钟，以去除表面氧化物。盐酸处理后，用去离子水清洗工作电极，并将其保存在丙酮中，以备进一步使用。

NO_3^- electroreduction measurements

The NO_3^- electroreduction measurements were carried out in a conventional H cell, in which anolyte (30 mL of 0.5 M H_2SO_4) and catholyte (30 mL of 0.5 M H_2SO_4 mixed with 0.1 M HNO_3) were separated by Nafion 115 membrane. Bi NPs/CFP, IrO_2 loaded Ti mesh, and Ag/AgCl were used as working electrode, counter electrode, and reference electrode, respectively. The

chronoamperometry electrolysis was controlled by an Autolab potentiostat/galvanostat (CHI660E). All potentials were measured vs. the Ag/AgCl reference electrode (vs. Ag/AgCl) and converted to the reversible hydrogen electrode reference scale (vs. RHE) without iR correction on account of the equation: E (vs. RHE) = E (vs. Ag/AgCl) + 0.21 V + 0.0591 × pH. During the process of NO₃⁻ electroreduction, the gaseous products in Ar stream were monitored by an online GC equipped with a flame ionization detector and a thermal conductivity detector once every five minutes. The liquid products were detected by ¹H NMR, where NH₂OH was captured by an excess amount of C₂H₂O₃ through oximation. Specifically, 0.4 mL of the catholyte after 1-h electrolysis was mixed with 0.1 mL of *d*₆-DMSO and 12.5 μL of 50wt% C₂H₂O₃. 0.1 mL of 6.0 mM DSS solution was added as an internal standard. The chronopotentiometry electrolysis at 100 mA cm⁻² (corresponding to -1.0 V vs. RHE) was conducted for both the continuous NO₃⁻ electroreduction and cyclic stability tests.

NO₃⁻ 电还原测量

NO₃⁻ 电还原测量在传统的 H 电解池中进行,在该电解池中,前溶液(30 mL 0.5 M H₂SO₄)和后溶液(30 mL 0.5 M H₂SO₄ 混合 0.1 M HNO₃)由 Nafion 115 膜隔开。Bi NPs/CFP、IrO₂ 负载钛网和 Ag/AgCl 分别用作工作电极、对电极和参比电极。计时器电解由 Autolab 恒电位仪/恒电流仪 (CHI660E) 控制。所有电位都是相对于银/氯化银参比电极 (vs. Ag/AgCl) 测量的,并根据等式转换为可逆氢电极参比刻度 (vs. RHE),不进行 iR 校正: E (vs. RHE) = E (vs. Ag/AgCl) + 0.21 V + 0.0591 × pH。在 NO₃⁻ 电还原过程中,配备火焰离子化检测器和热导检测器的在线气相色谱仪每五分钟对 Ar 流中的气态产物进行一次监测。液态产物通过 ¹H NMR 进行检测,其中 NH₂OH 通过氧化作用被过量的 C₂H₂O₃ 捕获。具体来说,将电解 1 小时后的 0.4 mL 电解液与 0.1 mL *d*₆-DMSO 和 12.5 μL 50wt% C₂H₂O₃ 混合。加入 0.1 mL 6.0 mM DSS 溶液作为内标。在 100 mA cm⁻² (对应于 -1.0 V vs. RHE) 的条件下进行计时电位计电解,以进行连续的 NO₃⁻ 电还原和循环稳定性测试。

The calculation of FE

The FE for a specific product was calculated according to equation 1:

$$FE = C_{\text{product}} \times V \times N \times F / Q \times 100\% \quad (1)$$

C_{product} : the measured concentration of a specific product, mole per liter (mol/L, M);

V : the volume of the electrolyte for liquid products and the total gaseous volume for gaseous products, liter (L);

N : the number of electron transfer for the formation of a specific product, 6, 8, and 2 for the formation of NH_2OH , NH_3 , and H_2 , respectively;

F : Faraday constant, 96485 C mol^{-1} ;

Q : quantity of electric charge, coulomb (C).

The calculation of the yield rate for NH_2OH

The yield rate for NH_2OH was calculated based on the following equation:

$$\text{yield rate}(\text{NH}_2\text{OH}) = n(\text{NH}_2\text{OH})/A/t \quad (2)$$

n : the accumulated molar quantity during t -h NO_3^- electroreduction, 10^{-6} mole (μmol);

A : the geometric area of the cathodic electrode, square centimeter (cm^2);

t : reaction time, hour (h).

The calculation of selectivity for NH_2OH

The selectivity for NH_2OH was calculated according to equation 3:

$$\text{Selectivity}(\text{NH}_2\text{OH}) = n(\text{NH}_2\text{OH})/[n(\text{NH}_2\text{OH})+n(\text{NH}_3)] \times 100\% \quad (3)$$

n : the accumulated molar quantity during a period of NO_3^- electroreduction, μmol .

DFT calculations

Spin-polarized periodic DFT calculations were performed using the Vienna Ab-Initio Simulation Package (VASP) code at the GGA level within the PAW-PBE formalism³³⁻³⁶. The van der Waals interactions were described using the empirical DFT+D3 method³⁷. The slab models of the four-layer Ni(100) facet, four-layer Cu(100) facet, four-layer Ag(100) facet, four-layer Sn(211) facet, four-layer Pt(100) facet, and two-layer Bi(012) facet were adopted with a vacuum of 15 \AA . The total energy calculations were performed using a $3 \times 3 \times 1$ grid and a plane wave with cut-off energy of 400 eV. Atoms in the bottom two layers were fixed and all other atoms including adsorbates were allowed to relax until the force on each ion was smaller than 0.02 eV \AA^{-1} .

The E_{ads} was defined as follow:

$$E_{\text{ads}} = E_{\text{adsorb-surf}} - E_{\text{surf}} - E_{\text{adsorb}} \quad (4)$$

where $E_{\text{adsorb-surf}}$, E_{surf} , and E_{adsorb} represent the total energies of the slab with adsorbate, the clean

slab, and the isolated adsorbate, respectively.

The Gibbs free energy change is defined as follow:

$$\Delta G = \Delta E + \Delta ZPE - T\Delta S \quad (5)$$

where ΔE is obtained from DFT calculations, ΔZPE represents the correction in zero-point energies, and $T\Delta S$ is the contribution of entropy. In this study, we use the nudged elastic band (NEB) method³⁷ to calculate the activation energy for the breaking of N-O bonds in *NH₂OH.

Instrumentations

SEM images and EDX elemental mapping images were obtained with a scanning electron microscope (SEM, JSM-6700F) operated at 5 kV. HAADF-STEM images were carried out on a JEOL ARM-200F field-emission transmission electron microscope operating at an accelerating voltage of 200 kV using Cu-based TEM grids. XRD patterns were recorded by using a Philips X'Pert Pro Super diffractometer with Cu- K_{α} radiation ($\lambda = 1.54178 \text{ \AA}$). XPS measurements were performed on a Kratos Axis Supra⁺ X-ray photoelectron spectrometer with an exciting source of Al $K_{\alpha} = 1486.6 \text{ eV}$. The gaseous products were monitored by an online gas chromatography (SHIMADZU, GC-2014). Liquid products were examined on a Varian 400 MHz NMR spectrometer (Bruker AVANCE AV III 400). The concentration of NO₃⁻ was quantitatively determined *via* an ion chromatography (Thermo Scientific, DIONES AX-DV). Raman spectroscopy measurements were carried out on a LabRAM HR Evolution (HORIBA Scientific).

Data Availability

All data that led us to understand the results presented here are available with the paper or from the corresponding author upon reasonable request.

References

1. Rosca, V., Duca, M., de Groot, M. T. & Koper, M. T. M. Nitrogen cycle electrocatalysis. *Chem. Rev.* **109**, 2209-2244 (2009).
2. Tabolin, A. A. & Ioffe, S. L. Rearrangement of N-oxyenamines and related reactions. *Chem. Rev.* **114**, 5426-5476 (2014).
3. Huang, H., Ji, X., Wu, W. & Jiang, H. Transition metal-catalyzed C-H functionalization of N-oxyenamine internal oxidants. *Chem. Soc. Rev.* **44**, 1155-1171 (2015).
4. Zhao, F. et al. A simple and efficient approach for preparation of hydroxylamine sulfate from the acid-catalyzed hydrolysis reaction of cyclohexanone oxime. *Chem. Eng. J.* **272**, 102-107 (2015).
5. Manente, F., Pietrobon, L., Ronchin, L. & Vavasori, A. Trifluoroacetic acid hydroxylamine system as organocatalyst reagent in a one-pot salt free process for the synthesis of caprolactam and amides of industrial interest. *Catal. Lett.* **151**, 3543-3549 (2021).
6. Tursun, M. & Wu, C. Single transition metal atoms anchored on defective MoS₂ monolayers for the electrocatalytic reduction of nitric oxide into ammonia and hydroxylamine. *Inorg. Chem.* **61**, 17448-17458 (2022).
7. Semon, W. L. The preparation of hydroxylamine hydrochloride and acetoxime. *J. Am. Chem. Soc.* **45**, 188-190 (1923).
8. Tauszik, G. R. & Crocetta, P. Production of hydroxylamine from nitrogen oxide: A short review. *Appl. Catal.* **17**, 1-21 (1985).
9. Benson, R. E., Cairns, T. L. & Whitman, G. M. Synthesis of hydroxylamine. *J. Am. Chem. Soc.* **78**, 4202-4205 (1956).
10. Shelef, M. & Graham, G. W. Why rhodium in automotive three-way catalysts? *Catal. Rev.* **36**, 433-457 (1994).
11. Murray, R. W. & Singh, M. A high yield one step synthesis of hydroxylamines. *Synth. Commun.* **19**, 3509-3522 (1989).
12. Mantegazza, M. A. & Leofanti, G. A one-step rapid synthesis of TS-1 zeolites with highly catalytically active mononuclear TiO₆ species. *Stud. Surf. Sci. Catal.* **82**, 541-550 (1994).
13. Tsegaw, Y. A. et al. Formation of hydroxylamine in low-temperature interstellar model ices. *J. Phys. Chem. A* **121**, 7477-7493 (2017).
14. Zecchina, A. et al. Structural characterization of Ti centres in Ti-silicalite and reaction

- mechanisms in cyclohexanone ammoximation. *Catal. Today* **32**, 97-106 (1996).
15. Wu, P., Komatsu, T. & Yashimal, T. Ammoximation of ketones over titanium mordenite. *J. Catal.* **168**, 400-411 (1997).
 16. Wu, Y., Jiang, Z., Lin, Z., Liang, Y. & Wang, H. Direct electrosynthesis of methylamine from carbon dioxide and nitrate. *Nat. Sustain.* **4**, 725-730 (2021).
 17. Liu, X., Jiao, Y., Zheng, Y., Jaroniec, M. & Qiao, S. Z. Mechanism of C-N bonds formation in electrocatalytic urea production revealed by ab initio molecular dynamics simulation. *Nat. Commun.* **13**, 5471 (2022).
 18. Zheng, T. et al. Upcycling CO₂ into energy-rich long-chain compounds via electrochemical and metabolic engineering. *Nat. Catal.* **5**, 388-396 (2022).
 19. Chen, G.-F. et al. Electrochemical reduction of nitrate to ammonia via direct eight-electron transfer using a copper-molecular solid catalyst. *Nat. Energy* **5**, 605-613 (2020).
 20. Chen, F.-Y. et al. Efficient conversion of low-concentration nitrate sources into ammonia on a Ru-dispersed Cu nanowire electrocatalyst. *Nat. Nanotechnol.* **17**, 759-767 (2022).
 21. Liu, Y. et al. A highly efficient metal-free electrocatalyst of F-doped porous carbon toward N₂ electroreduction. *Adv. Mater.* **32**, e1907690 (2020).
 22. Winter, L. R. & Chen, J. G. N₂ fixation by plasma-activated processes. *Joule* **5**, 300-315 (2021).
 23. Ren, Y. et al. Microscopic-level insights into the mechanism of enhanced NH₃ synthesis in plasma-enabled cascade N₂ oxidation-electroreduction system. *J. Am. Chem. Soc.* **144**, 10193-10200 (2022).
 24. Li, L. et al. Efficient nitrogen fixation to ammonia through integration of plasma oxidation with electrocatalytic reduction. *Angew. Chem. Int. Ed.* **60**, 14131-14137 (2021).
 25. Daems, N., Sheng, X., Alvarez-Gallego, Y., Vankelecom, I. F. J. & Pescarmona, P. P. Iron-containing N-doped carbon electrocatalysts for the cogeneration of hydroxylamine and electricity in a H₂-NO fuel cell. *Green Chem.* **18**, 1547-1559 (2016).
 26. Sheng, X. et al. Carbon-supported iron complexes as electrocatalysts for the cogeneration of hydroxylamine and electricity in a NO-H₂ fuel cell: A combined electrochemical and density functional theory study. *J. Power Sources* **390**, 249-260, (2018).
 27. Kim, D. H. et al. Selective electrochemical reduction of nitric oxide to hydroxylamine by atomically dispersed iron catalyst. *Nat. Commun.* **12**, 1856 (2021).

28. Zhang, X. et al. Direct electro-synthesis of valuable C=N compound from NO. *Chem Catal.* **2**, 1807-1818 (2022).
29. Wang, Y. et al. Enhanced nitrate-to-ammonia activity on copper–nickel alloys via tuning of intermediate adsorption. *J. Am. Chem. Soc.* **142**, 5702-5708 (2020).
30. Song, Z. et al. Efficient electroreduction of nitrate into ammonia at ultralow concentrations via an enrichment effect. *Adv. Mater.* **34**, 2204306 (2022).
31. Ye, S. et al. Elucidating the activity, mechanism and application of selective electrosynthesis of ammonia from nitrate on cobalt phosphide. *Energy Environ. Sci.* **15**, 760 (2022).
32. Kong, X. et al. Enhancing CO₂ electroreduction selectivity toward multicarbon products via tuning the local H₂O/CO₂ molar ratio. *Nano Lett.* **22**, 8000-8007 (2022).
33. Kresse, G. & Furthmüller, J. Efficiency of ab-initio total energy calculations for metals and semiconductors using a plane-wave basis set. *Comput. Mater. Sci.* **6**, 15-50 (1996).
34. Kresse, G. & Joubert, D. From ultrasoft pseudopotentials to the projector augmented-wave method. *Phys. Rev. B* **59**, 1758-1775 (1999).
35. Perdew, J. P., Burke, K. & Ernzerhof, M. Generalized gradient approximation made simple. *Phys. Rev. Lett.* **77**, 3865-3868 (1996).
36. Grimme, S., Ehrlich, S. & Goerigk, L. Effect of the damping function in dispersion corrected density functional theory. *J. Comp. Chem.* **32**, 1456 (2011).
37. Henkelman, G., Uberuaga, B. P. & Jonsson, H. A climbing image nudged elastic band method for finding saddle points and minimum energy paths. *J. Chem. Phys.* **113**, 9901-9904 (2000).

ACKNOWLEDGMENTS

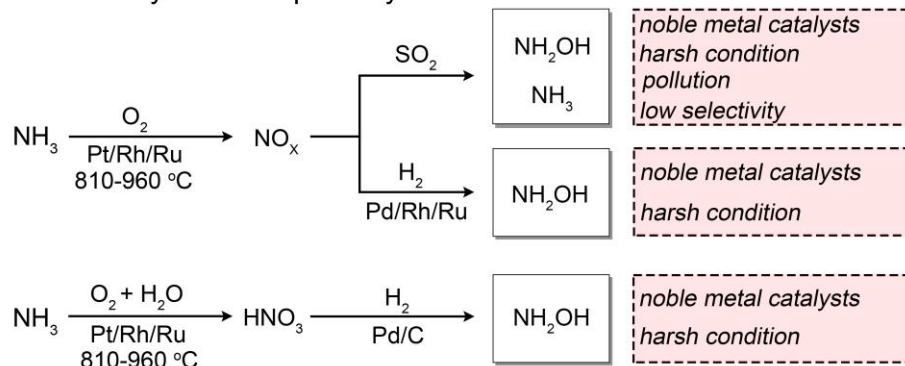
Funding: This work was supported by National Key Research and Development Program of China (2021YFA1500500 and 2022YFC2106000), Strategic Priority Research Program of the Chinese Academy of Sciences (XDB0450401), CAS Project for Young Scientists in Basic Research (YSBR-051 and YSBR-022), National Science Fund for Distinguished Young Scholars (21925204), National Natural Science Foundation of China (92061111, U19A2015, 22221003, 22250007, and 22209163), Fundamental Research Funds for the Central Universities, Provincial Key Research and Development Program of Anhui (202004a05020074), Collaborative

Innovation Program of Hefei Science Center, CAS (2022HSC-CIP004), the Joint Fund of the Yulin University and the Dalian National Laboratory for Clean Energy (YLU-DNL Fund 2022012), K. C. Wong Education (GJTD-2020-15), the DNL Cooperation Fund, CAS (DNL202003), Youth Project of Anhui Natural Science Foundation (2208085QB43), and USTC Research Funds of the Double First-Class Initiative (YD2340002002). This work was partially carried out at the USTC Center for Micro and Nanoscale Research and Fabrication.

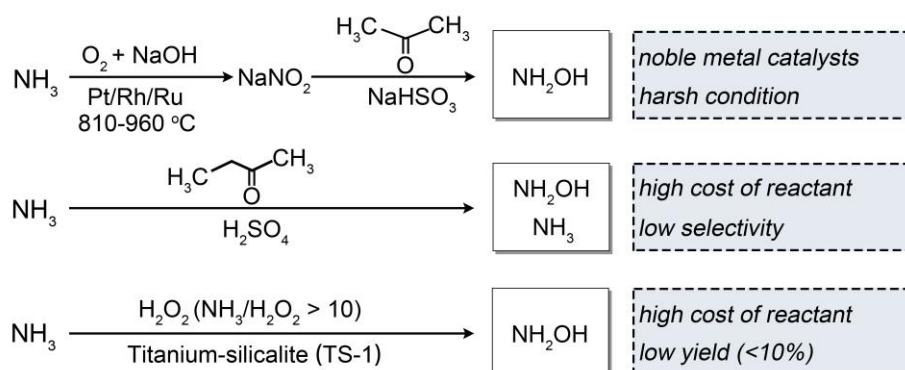
Author contributions: X.K. and J.N. contributed equally to this work. J.Z., Z.G., and X.K. conceived the idea and co-wrote the paper. X.K. and J.N. synthesized catalysts, conducted structural characterizations, and performed electroreduction tests with the help of J.Zheng and Z.X.. Z.S. and X.K. designed the plasma discharge device and performed the N₂ plasma fixation tests with the help of L.Q.. Z.Y. performed the theoretical calculations. H.L. made suggestions on the paper. All authors discussed the results and commented on the manuscript.

Competing interests: The authors declare no financial interests.

a Traditionally industrial pathways



b Newly emerging pathways



c Plasma-electrochemical cascade pathway (this work)

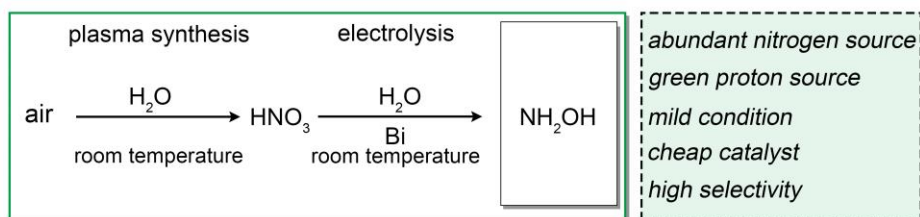


Fig. 1 | Schematic illustration of the synthetic pathways for NH₂OH. **a-c**, The traditionally industrial pathways (**a**), the newly emerging pathways (**b**), and the sustainable PECP from the ambient air and H₂O (**c**).

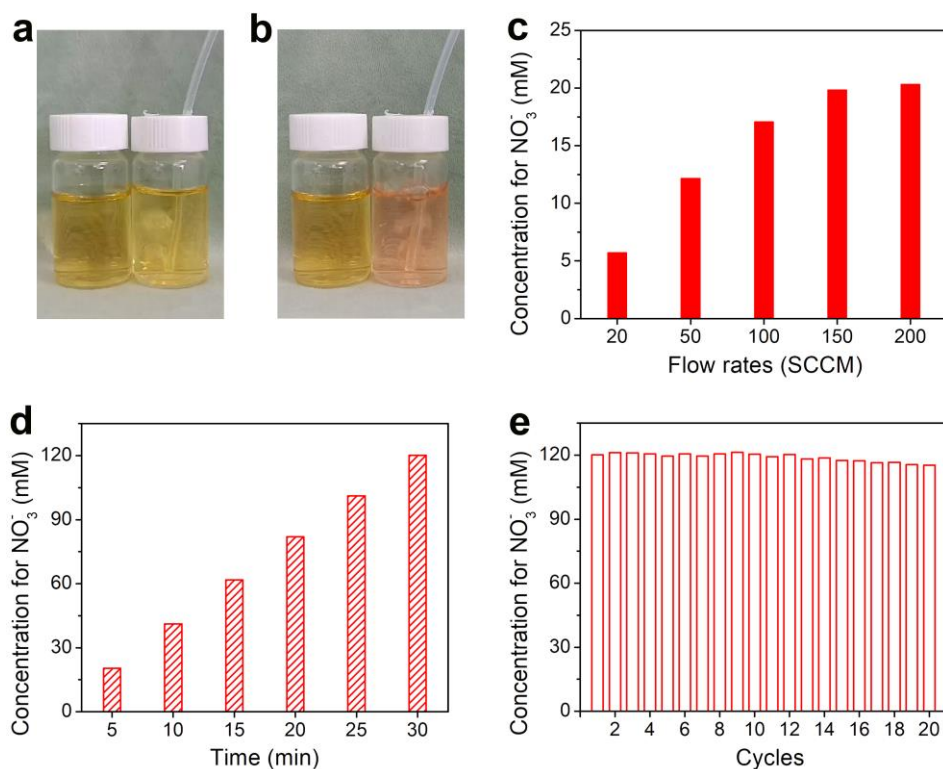


Fig. 2 | Plasma synthesis of NO_3^- from the ambient air and H_2O . **a,b**, The photographs of the pristine absorbent (**a**) and the absorbent after absorbing the gaseous substances produced by the plasma discharge device for 30 s (**b**). The vials on the left and right sides were used as control and experiment groups, respectively. **c**, The concentration for NO_3^- in 30 mL of absorbent under various flow rates of ambient air for a 5-min discharge. **d**, The accumulated concentration for NO_3^- in 30 mL of absorbent under the flow rate of 200 SCCM for various discharge times. **e**, Cyclic stability for NO_3^- production in 30 mL of absorbent under the flow rate of 200 SCCM with each cycle for a 30-min continuous discharge.

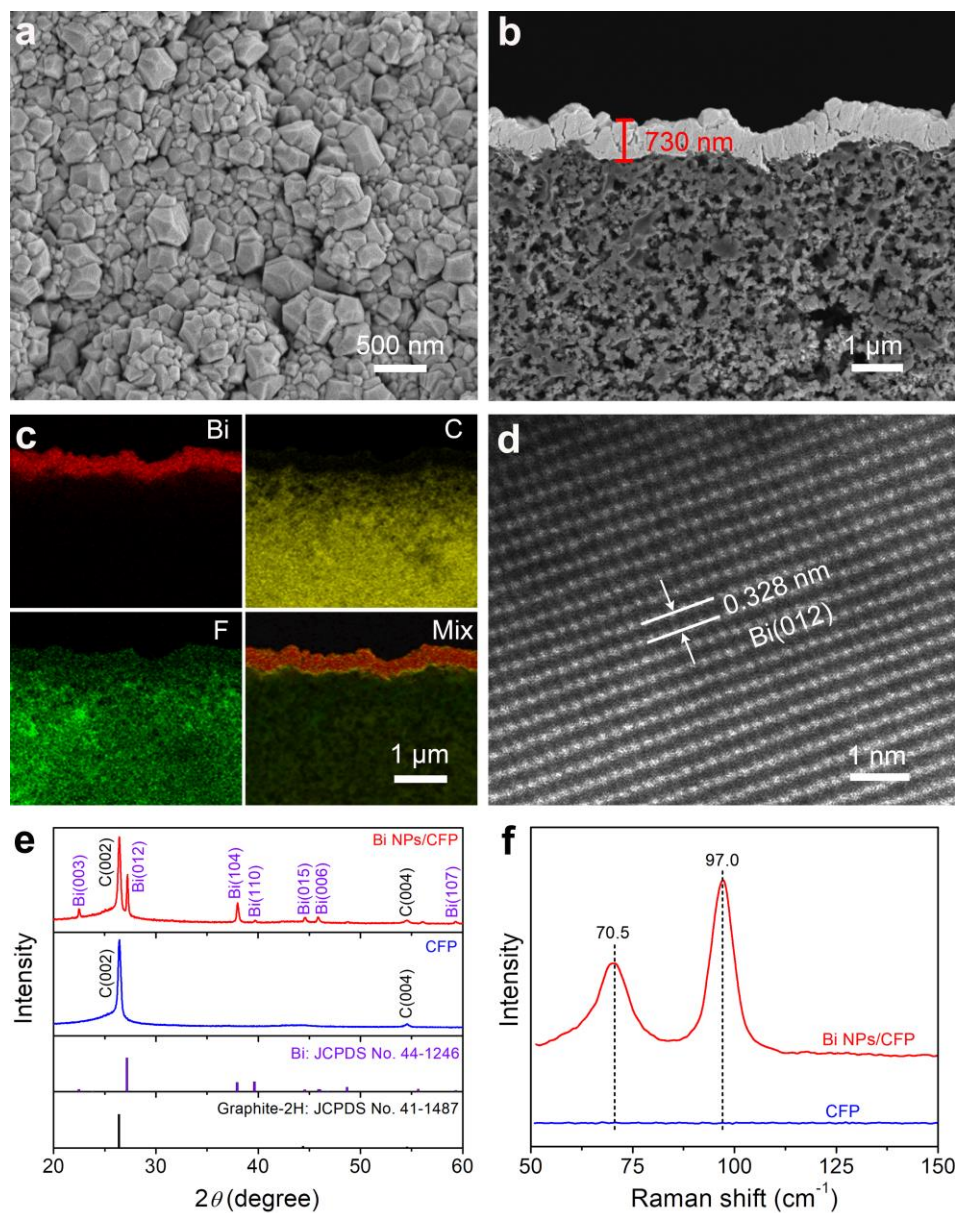


Fig. 3 | Characterizations of Bi NPs/CFP catalyst. **a**, SEM image of Bi NPs/CFP. **b,c**, SEM image (**b**) and SEM-EDX elemental mapping images (**c**) of the cross-sectional Bi NPs/CFP. **d**, HAADF-STEM image of an individual Bi nanoparticle in Bi NPs/CFP. **e,f**, XRD patterns (**e**) and Raman spectra (**f**) of both Bi NPs/CFP and CFP.

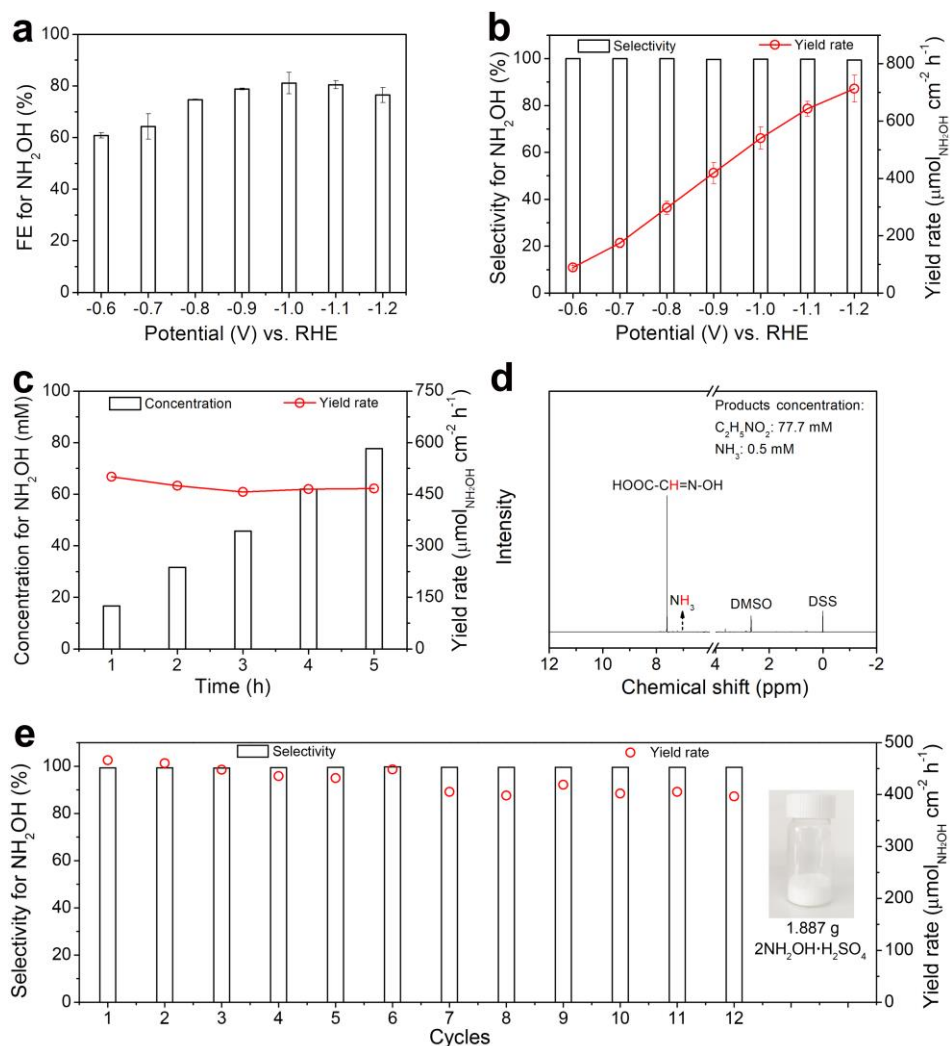


Fig. 4 | Catalytic performance of NO_3^- electroreduction over Bi NPs/CFP. **a,b**, FE for NH_2OH (**a**) and the selectivity/yield rate for NH_2OH (**b**) towards NO_3^- electroreduction over Bi NPs/CFP. **c**, The accumulated concentration and yield rate for NH_2OH during the 5-h continuous electrolysis. **d**, ^1H NMR spectrum of the electrolyte after the 5-h continuous electrolysis with the addition of 0.2 M $\text{C}_2\text{H}_2\text{O}_3$. **e**, Cyclic stability test towards NO_3^- electroreduction over Bi NPs/CFP with each cycle for a 5-h continuous electrolysis. Insert Fig. 4e shows the solid $2\text{NH}_2\text{OH} \cdot \text{H}_2\text{SO}_4$ products separated after 12 cyclic tests of NO_3^- electroreduction.

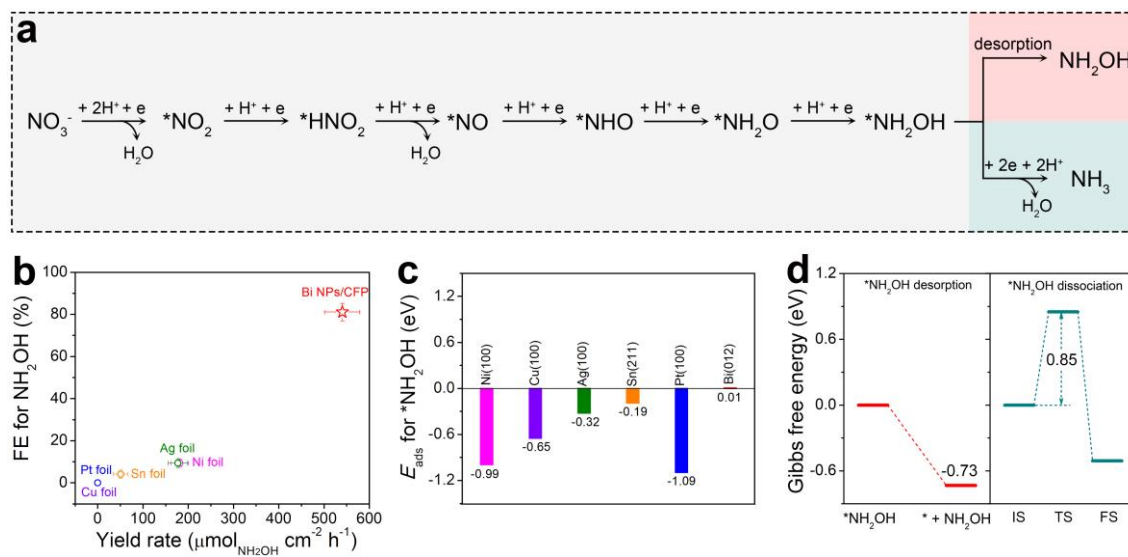


Fig. 5 | Mechanistic study of NO_3^- electroreduction into NH_2OH . **a**, A typical reaction pathway for NH_2OH and NH_3 towards NO_3^- electroreduction. **b**, FE for NH_2OH plotted against yield rate for NH_2OH over various metallic catalysts at -1.0 V vs. RHE. **c**, E_{ads} for $\text{*NH}_2\text{OH}$ on various metallic surfaces. **d**, Gibbs free energy diagram for $\text{*NH}_2\text{OH}$ desorption and $\text{*NH}_2\text{OH}$ dissociation on the Bi(012) facet.